ACS Partner Journal

CHEMICAL & BIOMEDICAL IMAGING

Open Access

pubs.acs.org/ChemBioImaging

Article

Multiplexed and Millimeter-Scale Fluorescence Nanoscopy of Cells and Tissue Sections via Prism-Illumination and Microfluidics-Enhanced DNA-PAINT

Matthew J. Rames, John P. Kenison, Daniel Heineck, Fehmi Civitci, Malwina Szczepaniak, Ting Zheng, Julia Shangguan, Yujia Zhang, Kai Tao, Sadik Esener, and Xiaolin Nan*

Cite This: *Chem. Biomed. Imaging* 2023, 1, 817−830

Read Online

ACCESS | Metrics & More | Article Recommendations | Supporting Information

ABSTRACT: Fluorescence nanoscopy has become increasingly powerful for biomedical research, but it has historically afforded a small field-of-view (FOV) of around 50 μm × 50 μm at once and more recently up to ∼200 μm × 200 μm. Efforts to further increase the FOV in fluorescence nanoscopy have thus far relied on the use of fabricated waveguide substrates, adding cost and sample constraints to the applications. Here we report PRism-Illumination and Microfluidics-Enhanced DNA-PAINT (PRIME-PAINT) for multiplexed fluorescence nanoscopy across millimeter-scale FOVs. Built upon the well-established prism-type total internal reflection microscopy, PRIME-PAINT achieves robust single-molecule localization with up to ∼520 μm × 520 μm single FOVs and 25−40 nm lateral resolutions. Through stitching, nanoscopic imaging over mm^2 sample areas can be completed in as little as 40 min per target. An on-stage microfluidics chamber facilitates probe exchange for multiplexing and enhances image quality, particularly for formalin-fixed paraffin-embedded (FFPE) tissue sections. We demonstrate the utility of PRIME-PAINT by analyzing ∼10^6 caveolae structures in ∼1,000 cells and imaging entire pancreatic cancer lesions from patient tissue biopsies. By imaging from nanometers to millimeters with multiplexity and broad sample compatibility, PRIME-PAINT will be useful for building multiscale, Google-Earth-like views of biological systems.

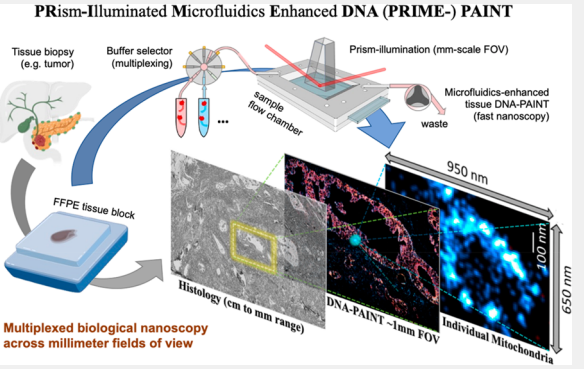

KEYWORDS: *fluorescence nanoscopy, super-resolution microscopy, DNA-PAINT, large field-of-view, multiscale imaging, tissue sections, prism-illumination, microfluidics*

INTRODUCTION

Advances in super-resolution microscopy techniques such as PALM,[1,2] STORM,[3] PAINT (including DNA-PAINT),[4,5] STED,[6] and their relatives[7,8] in the recent decades have pushed the effective resolution of optical microscopy to ∼20 nm or better, providing unparalleled insights into biological structures and processes at the molecular scale. Until very recently, however, the various fluorescence nanoscopies have afforded rather small FOVs, commonly ∼50 μm × 50 μm in the lateral dimensions, addressing only a few cells at once. This has limited the utility of fluorescence nanoscopy in studying complex and heterogeneous biological systems, for example, multicellular structures in model systems or clinical samples, which can comprise hundreds of cells or more and span millimeters and beyond.

Emerging research has begun to tackle this issue. Huang et al. used a high power illumination scheme to obtain FOVs up to ∼200 μm × 200 μm with STORM.[9] In this case, an ∼6 W laser power (at 640 nm) was necessary for efficient fluorophore photoswitching across such large illumination areas. Utilizing a sophisticated line-scanning illumination scheme termed "ASTER", Mau et al. also reached FOVs up to ∼200 μm × 200 μm at a moderate laser power (∼250 mW) for both STORM and DNA-PAINT.[10] As in most fluorescence nanoscopies, these methods employed the popular, through-objective imaging scheme where the same, high numerical aperture (NA > 1.4) objective supports both sample illumination and signal collection. Despite the high signal collection efficiency and resolving power of these objective lenses, the best achievable FOV is typically not more than ∼200 μm × 200 μm, beyond which optical aberrations and beam geometry constraints become limiting. At this FOV, tens of (5 × 5 or more) FOVs need to be stitched to reach the

Received: May 19, 2023
Revised: July 24, 2023
Accepted: August 18, 2023
Published: October 12, 2023

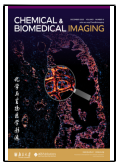

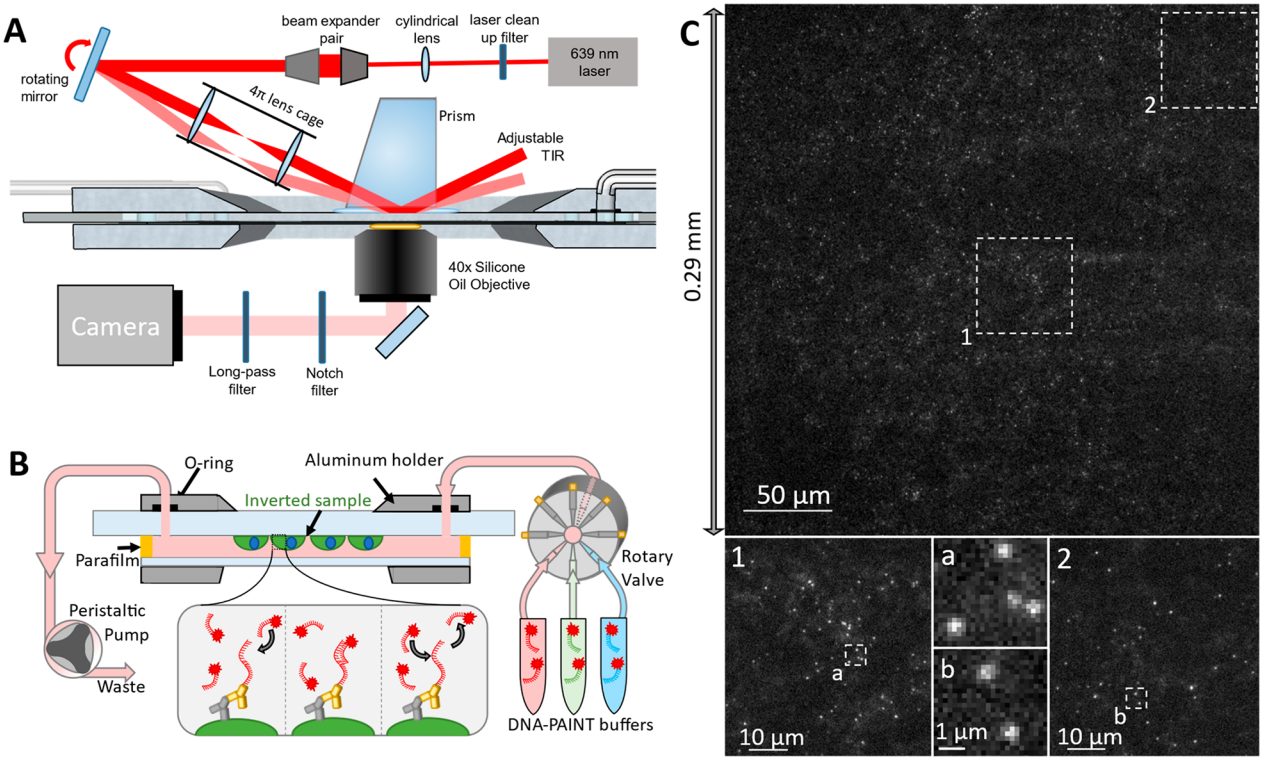

Figure 1. Overview of PRIME-PAINT optics, fluidics, and example single-molecule images. (A) Schematic of the PRIME-PAINT microscope design and general imaging strategy, with the widened laser beam and controllable TIR angle. (B) Schematic cross-section of the flow chamber assembly and sample position. Notably, cultured cells/mounted tissue are attached on an inverted sample coverslide, enabling both encapsulation of imaging solutions and buffer exchange for multitarget DNA-PAINT imaging. DNA-PAINT imaging utilizes affinity agents such as antibodies (in yellow) conjugated to DNA oligonucleotides (red, referred to as docking strands or DS) and complementary imaging strands (IS, shown in red with a fluorophore represented by a red star) to provide transient single-molecule localizations while freely diffusing strands contribute only slightly to background fluorescence. (C) Representative PRIME-PAINT raw image at 30 ms exposure highlights single-molecule localization quality. Single-molecule events are clearly resolved both in the center on the FOV and near the corners, exemplifying the 300 μm × 300 μm FOV.

millimeter scale, which will still take hours to days to complete even for a single target.

Even larger FOVs in fluorescence nanoscopies would likely need to involve imaging schemes in which separate light paths are used for sample illumination and signal detection. Indeed, several recent reports based on planar waveguides have demonstrated FOVs of up to ~0.5 mm × 0.5 mm. These methods employ high-refractive-index contrast (HIC) materials such as Ta_2O_5 or Si_3N_4[11−13] grown on silicon or polymer[14] deposited on clear glass to create a thin, planar waveguide as the imaging substrate. Excitation light is coupled to the waveguide from the side using specialized optics (e.g., a dedicated objective lens) to generate a continuous, evanescent field to illuminate the sample along the beam path. The fluorescence signal can be collected using an objective of choice, allowing for imaging at different magnifications and resolution levels. Typically, by using a high power (e.g., 60× and NA 1.2−1.5) objective, lateral resolutions of ~50 nm could be achieved (e.g., with STORM) over a smaller (~200 μm × 200 μm) FOV.[11−13] Larger FOVs up to ~0.5 mm × 0.5 mm could be obtained at a lower magnification and NA (e.g., 25× and NA 0.8), with lateral resolutions in the 70−200 nm range.[13] The platform is also compatible with other sub-diffractive imaging modalities such as super-resolution radial fluctuation (SRRF).[14]

Despite the impressive FOVs with chip-based nanoscopy, routine use of this platform in most biomedical laboratories can be faced with several hurdles, with the first being the need for using microfabricated HIC waveguides and dedicated alignment optics for light coupling. By design, the input light also needs to be under total internal reflection (TIR) throughout the entire light path, which will limit the use under nonstrict TIR illumination conditions. The light-coupling optics (e.g., the objective lens) often needs to be mechanically dithered to overcome interference patterns due to repeated reflections of light at the interface.[12] An additional consideration is the sample compatibility. While the waveguide substrates have shown good performance on cultured cells and cryo-preserved tissue sections,[15] its applications to formalin-fixed paraffin-embedded (FFPE) tissue sections, the most common clinical sample format, remain to be developed. In previous work, we and others have demonstrated the utility of fluorescence nanoscopy in revealing structural and molecular details such as chromatin organization in early cancer progression[16] and mitochondria organization[17] from FFPE sections. Extending fluorescence nanoscopy to FFPE tissue sections with large-field capability in ways that can be seamlessly integrated into current standard workflows would be of immense value.

To address these needs, we have developed a microscope platform for multiplexed imaging of cells and clinical tissue samples with DNA-PAINT across up to ~0.5 mm × 0.5 mm FOVs in a single acquisition. This platform, which we termed PRism-Illumination and Microfluidics-Enhanced (PRIME-) PAINT, utilizes a prism-based illumination scheme that can be easily implemented on common inverted fluorescence

https://doi.org/10.1021/cbmi.3c00060
Chem. Biomed. Imaging 2023, 1, 817−830

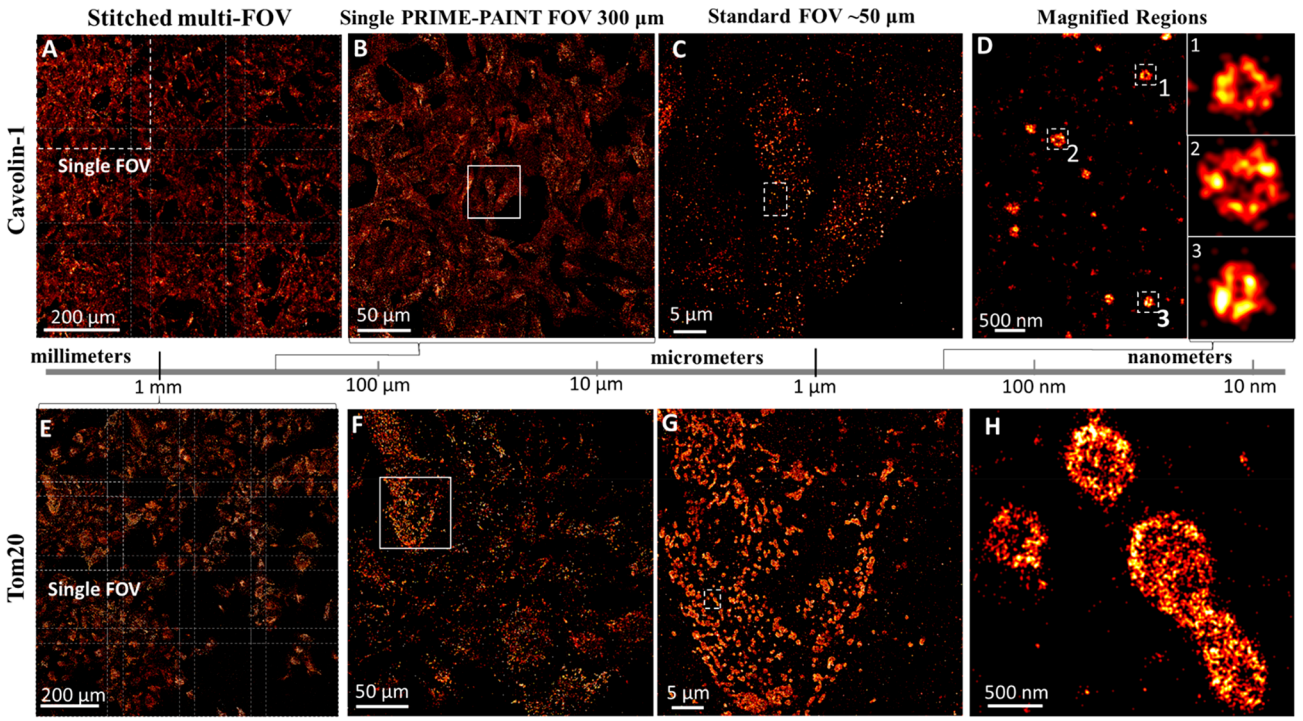

Figure 2. PRIME-PAINT imaging of caveolae and mitochondria over millimeter FOVs in U2OS cells. Representative single and stitched PRIME-PAINT images of membrane-adjacent caveolae (A–D) and cytosolic Tom20 (E–H). (A) Stitched 3 × 3 array of membrane-adjacent caveolae at 800 μm × 800 μm FOV with 40 μm overlaps. (B) Single PRIME-PAINT FOV at nearly 300 μm × 300 μm of Caveolin-1 imaged with a strict TIR angle. (C) Magnified region from part B highlighting the detail within a more standard smaller FOV of ~50 μm. (D) Magnified cell region from part C and three insets showing high-quality super-resolution detail of caveolae vesicles. (E) Stitched 4 × 4 array of cytosolic Tom20 over 1 mm^2. (F) Single PRIME-PAINT FOV at nearly 300 μm × 300 μm. (G) Magnified region from part F highlighting mitochondria within a more standard smaller FOV of ~50 μm. (H) Magnified cell region from part G with distinct mitochondria. Each single PRIME-PAINT image (B, F) was acquired in 15 min (30,000 frames at 30 ms exposure) using 1 nM IS2-ATTO643 and 12.5% EC for both Caveolin-1 and Tom20. The stitched 3 × 3 FOV for caveolae was acquired in 135 min, while the 4 × 4 FOV for Tom20 was acquired in 240 min. Scale bars are 200 μm in parts A and E, 50 μm in parts B and F, 5 μm in parts C and G, and 500 nm in parts D and H. The insets in part D are 300 nm wide.

microscopes with off-the-shelf optical components. PRIME-PAINT affords FOVs equivalent to chip-based nanoscopy but maintains spatial resolutions comparable to those of through-objective systems. Multiplexed, nanoscopic imaging via exchange-PAINT is facilitated using an integrated microfluidic sample chamber, which was critical to high quality imaging of clinical FFPE tissue sections through microfluidics-enhanced DNA-PAINT. We demonstrate multicolor imaging of both cultured cells and clinical FFPE sections with nanometer (typically 25–40 nm) spatial resolutions. Enabled by the dramatically increased data throughput, we used machine-learning-based image segmentation and quantitation of the resulting, multiscale nanoscopic images, offering new insights into nanostructures and molecular interactions across larger cell populations. Collectively, we present PRIME-PAINT as a novel approach to the high-resolution and high-throughput spatial mapping of cells and clinical samples across the scales from molecules to multicellular systems.

RESULTS

Integrating Prism-Type Illumination and Microfluidics with DNA-PAINT

PRIME-PAINT combines a prism-type illumination scheme with an on-stage microfluidic system for programmable fluid exchange. This combination was essential to enable multiplexed fluorescence nanoscopy via exchange-PAINT over much larger FOVs compared with prior configurations. We chose DNA-PAINT as the primary nanoscopy method in this work because of its convenient multiplexing through exchange-PAINT[5] and robust multi-FOV stitching without probe loss during imaging.[18] In this work, we specifically used DNA-PAINT-ERS,[19,20] our improved implementation of DNA-PAINT, where the combination of ethylene carbonate (EC, as an imaging buffer additive), repetitive docking sequences, and a spacer between the affinity agent and the docking strand (DS) oligo enables fast and high-quality DNA-PAINT without needing strong laser excitation. Although not yet tested, the platform should also be compatible with other accelerated implementations of DNA-PAINT.[21−23]

Two TIR configurations, namely, prism-illumination[24] and through-objective,[25] are widely used for single-molecule imaging; both are also compatible with highly inclined laminar optical (HiLo) microscopy. Of the two, prism-illumination does not rely on TIR-capable objectives and thus is more flexible on the achievable FOV. Of note, current prism-illumination setups for single-molecule imaging still use high NA (commonly 60× oil, NA = 1.4 or above) objectives and deliver FOVs around 50 μm × 50 μm. In our implementation, the laser first passes a pair of beam expanders, one of which is installed in reverse, to yield a collimated beam of adjustable size (Figure 1A). A cage-mounted 4f lens pair was placed between a rotatable mirror and the prism such that the FOV center remained static when rotating the mirror to adjust the incident angle of the beam. This setup allowed us to continuously adjust the illumination beam size between tens

https://doi.org/10.1021/cbmi.3c00060
Chem. Biomed. Imaging 2023, 1, 817−830

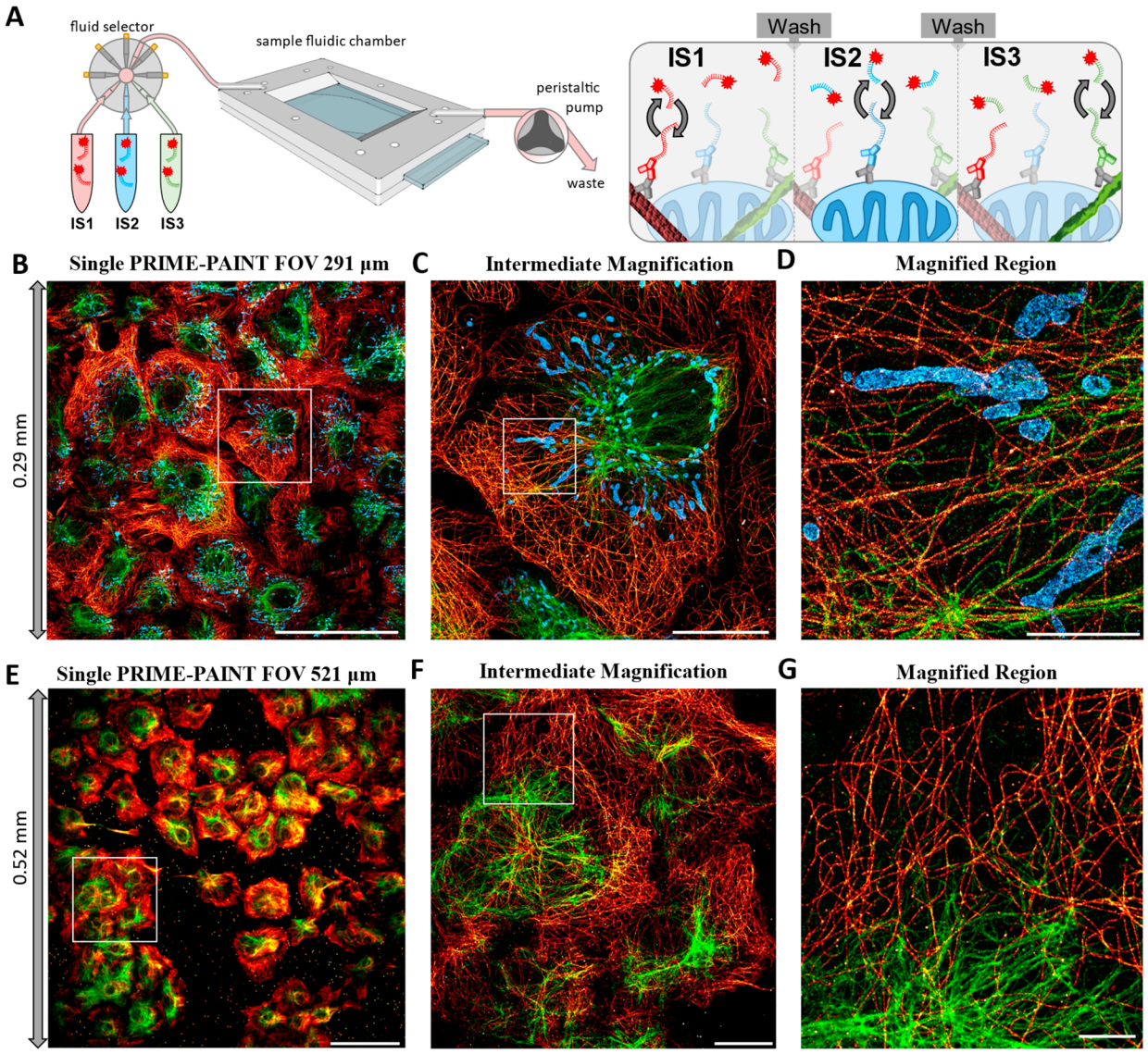

Figure 3. Multiplexed PRIME-PAINT imaging of cells via microfluidic exchange-PAINT. (A) Schematic of multiplexed imaging with complementary imaging strand (IS) targeting docking strand (DS) to microtubules (red), mitochondria (blue), and vimentin (green). (B) Single PRIME-PAINT three-target image of Cos7 cells at 300 μm × 300 μm. (C) Magnified region from part B highlighting image quality over a more standard ∼50 μm FOV. (D) Magnified region from part C showing distinct cytoskeletal structures and mitochondria. (E) Expanded PRIME-PAINT two-target FOV at 521 μm × 521 μm. (F) Intermediate magnification from part E at 100 μm FOV. (G) Magnified region from part F highlighting dense perinuclear vimentin and extended microtubule networks. The representative three-target image (B−D) was acquired in 45 min total (30,000 frames at 30 ms exposure for each target) using 1 nM IS1-ATTO643 and 12.5% EC, 1 nM IS2-ATTO643 and 12.5% EC, and 500 pM IS3-ATTO643 and 13.75% EC for microtubules, mitochondria, and vimentin, respectively. An expanded PRIME-PAINT FOV two-target image (E−G) was acquired in 30 min total (30,000 frames at 30 ms exposure for each target) using 1 nM IS1-ATTO643 and 12.5% EC and 500 pM IS3-ATTO643 and 13.75% EC for microtubules and vimentin, respectively. Scale bars are 100 μm in parts B and E, 20 μm in parts C and F, and 5 μm in parts D and G.

of micrometers and millimeters as well as to switch between TIR and HiLo modes without needing to recenter the FOV. By using a collimated incident beam and the 4f lens pair, typically only minor adjustments to the TIR angle (via the rotating mirror) are necessary even when switching to a new sample with a different refractive index. Lastly, the setup avoids focusing of high lasers onto sensitive optical surfaces (e.g., the back of an objective lens) and thus can accommodate more incident power if needed (Figure 1A).

With sample illumination decoupled from signal detection, we could choose objective lenses best suited for single-molecule detection across large FOVs and at long working distances (Figure 1A,B). We found that, on our setup, a 40× silicone (Sil) immersion objective[26] (NA 1.25) outperformed the more commonly used 60× oil immersion objective (NA = 1.4). Despite the lower NA, the Sil objective yielded nearly identical single-molecule brightness as the oil objective, while affording a lower background and better overall signal-to-noise ratio. Using the Prime 95B sCMOS with matching (60×) magnifications, the image quality started to deteriorate beyond the central ∼100 μm × 100 μm region with the oil objective but remained uniform across the entire 291 μm × 291 μm FOV with the Sil objective (Figure S1 and Figure 1C). By switching to another sCMOS, the Kinetix, we achieved an even

https://doi.org/10.1021/cbmi.3c00060
Chem. Biomed. Imaging 2023, 1, 817−830

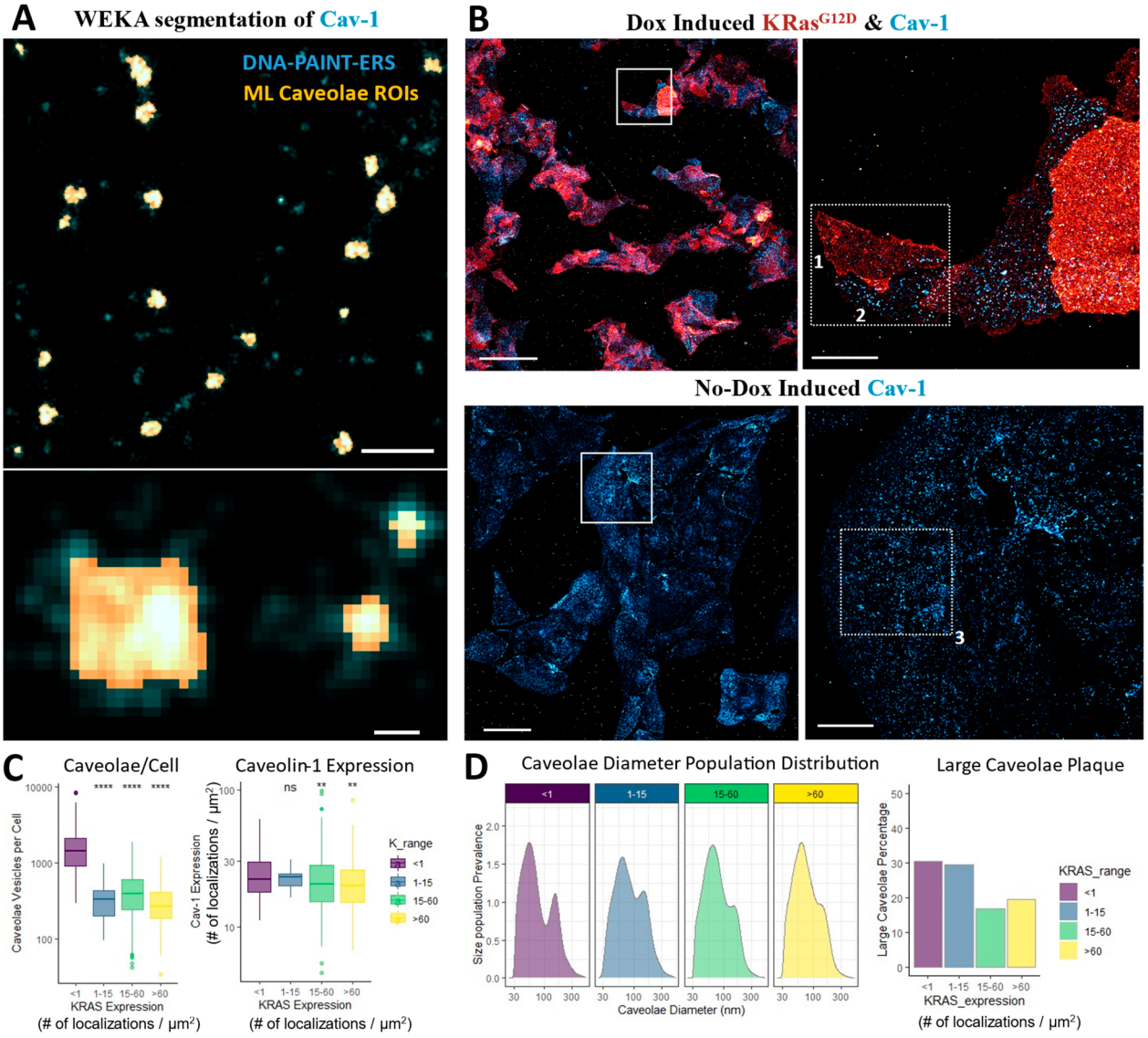

Figure 4. PRIME-PAINT image analysis of KRas G12D and caveolae in U2OS cells. (A) Representative overlays showing both caveolae vesicles as imaged via PRIME-PAINT in blue with corresponding caveolae outlines identified via machine learning segmentation in yellow (top). Inset showing both larger caveolae plaques and punctate caveolae vesicles, at ∼150 nm and ∼60 nm wide, respectively (bottom). (B) Representative PRIME-PAINT images of both dox-induced and non-dox-induced KRas G12D and Caveolin-1. KRas G12D labeled via SNAP-tag DS-1 conjugate shown in red, with Caveolin-1 DS2 shown in blue. Magnified regions show representative cells numbered 1, 2, and 3 with higher, lower, and no KRas G12D expressions, respectively. Manually annotated cell boundaries were subsequently input into a custom Fiji macro for both KRas G12D expression and WEKA classification of caveolae vesicles per cell. (C) Boxplot of the abundance of quantified caveolae vesicles versus ranges of mutant KRas expression (in units of no. of localizations/μm^2) for non-dox (<1), 1−15, 15−60, and >60 mutant KRas/μm^2. Boxplot of total Caveolin-1 expression versus ranges of mutant KRas expression per cell, with both expression values shown in no. of localizations/μm^2. (D) Population analysis of caveolae diameters for indicated KRas expression ranges, notably showing two main peaks at ∼60 nm and ∼150 nm from non-dox induction. The *Y*-axis is the relative population of caveolae at differing diameters on the *X*-axis (log10 scaled). Higher KRas G12D expression anticorrelates with the larger caveolae size population. Analysis was performed on 10 images of dox-induced and two images of non-dox-induced cells acquired with 30,000 frames at 30 ms exposure for each target, using 1 nM IS1-ATTO643 and 12.5% EC and 500 pM IS2-ATTO643 and 13.75% EC for KRas G12D-SNAP-DS1 and Caveolin-1-DS2, respectively. Scale bars in part A are 50 μm for full FOV images (left for each cell condition), 10 μm for matching magnified views (right), and 5 μm for all example cells (bottom panels). Plots in parts B and C were generated using the ggplot package in R. Significance levels (in part B) were calculated using the Wilcoxon test from average values within each cell relative to the non-dox-induced cells group.

larger FOV of 521 μm × 521 μm with comparable single-molecule image quality (Figure S2).

To accommodate this imaging configuration, the samples are sandwiched between a glass slide and a coverglass with the space in between filled with imaging buffer. We designed a microfluidic flow cell with a tear-drop shape for efficient and complete buffer exchange in multiplexed DNA-PAINT (exchange-PAINT),[5] inspired by previously demonstrated designs.[27] Fire-polished glass slides with low background could be directly used with conventional tissue cell-culture or coated with polyethylenimine (PEI) for use with FFPE tissue sections (see the Materials and Methods). Stretched and molten parafilm was used as a thin (∼35 ± 5 μm) spacer and a robust, hydrophobic seal. An optional custom holder (see the

https://doi.org/10.1021/cbmi.3c00060
Chem. Biomed. Imaging 2023, 1, 817−830

CAD file, Supporting Information) helps support and position the sample chamber on the microscope stage with improved mechanical stability. Finally, inlet and outlet fluid ports were connected to a rotary valve and a peristaltic pump, allowing manual or programmable fluid exchange during the imaging (Figure 1B).

Multiplexed PRIME-PAINT for Membrane and Cytosolic Targets in Cultured Cells

High-quality single-molecule imaging with PRIME-PAINT enabled large-field, nanoscopic imaging of cellular targets in cultured cells with single FOVs of ∼0.3 mm × 0.3 mm (Figure 2) or ∼0.5 mm × 0.5 mm (Figures S2 and S3). Imaging can be altered between membrane (such as caveolin; Figure 2A−D) and cytosolic (such as mitochondria; Figure 2E−H) targets by switching between the TIR and HiLo imaging modes, respectively. The acquisition time for each single FOV was ∼10−20 min (20−60k frames at 20−40 ms/frame) by leveraging the improved imaging kinetics afforded by DNA-PAINT-ERS.[19]

The use of DNA-PAINT(-ERS) allowed the robust stitching of multiple FOVs to address even larger sample areas. In Figure 2A, we demonstrate a 3 × 3 stitching (with an ∼40 μm overlap) with a combined FOV of 0.8 × 0.8 mm^2 in 1−2 h when imaging caveolae, and in Figure 2E, a 4 × 4 stitching with a combined FOV of 1 mm^2 in 2−4 h and when imaging mitochondria (10−15 min per single FOV in each case). Leveraging the larger ∼0.5 mm × 0.5 mm FOV enables imaging across ∼1 mm^2 as 2 × 2 stitches in under 40 min (Figure S3). We note that, at present, the stitched views are based on coarse alignments between matching gold fiduciaries in the overlapping regions. Optimal stitching with sub-diffractive registration precisions[28] (on par with the image resolutions) requires that the optical aberrations are properly corrected first[29,30] and is currently under development. Imaging of the same 1 mm^2 FOVs would have taken 1−3 days if using DNA-PAINT with a standard 50 μm × 50 μm FOV or 6−8 h even with ASTER.[10] Thus, PRIME-PAINT with DNA-PAINT-ERS[19] substantially increases imaging throughput compared with existing strategies.

We estimated the effective resolution of PRIME-PAINT by measuring the width of microtubules. For these estimates, we assumed the width of microtubules to be around 40 nm (considering the inherent width and size of the antibodies and the attached DS oligo). Microtubules exhibited full width at half-maxima (fwhm) of 47 ± 3 nm (objective-type DNA-PAINT-ERS) and 51 ± 4 nm (PRIME-PAINT at 0.3 mm × 0.3 mm FOV; see Figure S4). These correspond to an effective resolution of ∼25 nm for the objective-type DNA-PAINT, consistent with our previous results,[19] and slightly lower (∼30 nm) for PRIME-PAINT at 0.3 mm × 0.3 mm FOV using the Prime 95B camera. Imaging with the largest ∼0.5 mm × 0.5 mm FOVs yields a lower lateral resolution of 40−45 nm (fwhm ∼60 nm; Figure S4). The decrease in resolution is primarily due to the much-decreased laser power density, and using a more powerful (2−3 W; currently ∼1 W) laser should bring the resolution to the 20−30 nm range. In this work, we primarily used the 0.3 mm × 0.3 mm FOV to ensure optimal spatial resolution (∼30 nm).

The integrated microfluidics (Figure 1B) facilitated multiplexed PRIME-PAINT imaging by allowing for manual or programmed buffer exchange. For example, we labeled microtubules, mitochondria, and vimentin in cultured COS7 cells and imaged the three targets sequentially using exchange-PAINT (Figure 3A and B). A quick washing step between the imaging cycles by flowing in a blank imaging buffer (e.g., PBS with 15% EC) effectively eliminated any residual localizations within seconds without affecting the underlying structures (Figure S5). In the co-registered multitarget images (∼0.3 mm × 0.3 mm FOV), all three targets were well resolved, revealing their spatial relationships such as occasional associations between mitochondria and the two cytoskeletal filaments (Figure 3C,D). We similarly obtained a two-target PRIME-PAINT image of microtubules and vimentin over the larger 0.5 mm × 0.5 mm FOV (Figure 3E−G).

Imaging and Machine Learning Analysis of Nanostructures in Large Cell Populations

The high imaging throughput and resolution of PRIME-PAINT offer unique opportunities to analyze protein localizations and biological nanostructures across large cell populations. As a proof of concept, we analyzed caveolae in U2OS cells expressing KRas^{G12D}, an oncogenic mutant of KRas. In initial observations, we found that cells expressing high KRas^{G12D} levels appeared to have fewer and/or smaller caveolae (Figure 4A,B); we thus sought to further investigate this by leveraging the ability of PRIME-PAINT to quantitate the size and abundance of the caveolae in hundreds to thousands of cells at once.

The U2OS cells were engineered to express SNAP-KRas^{G12D} upon doxycycline (dox) induction,[31] where SNAP-KRas^{G12D} was labeled using DNA oligo-conjugated SNAP substrate (see the Materials and Methods) and caveolae with antibodies as described earlier (Figure 2A−D). We obtained and analyzed two-color images of mutant KRas and Caveolin-1 across 12 FOVs (∼0.3 mm × 0.3 mm), 10 of which were from Dox-induced (KRas^{G12D}-positive) cells and 2 from uninduced cells (KRas^{G12D}-negative). Next, we utilized WEKA,[32] an open-source platform for machine-learning with a built-in plugin for Fiji,[33] for automated identification and analysis of nanostructures from PRIME-PAINT images. As reconstructed PRIME-PAINT images were massive (∼30,000 × 30,000 pixels at 10 nm/pixel rendering from a single ∼0.3 mm × 0.3 mm FOV), we developed a Fiji macro to subdivide, classify, and quantitate the nanostructures and recombine the quantitation results (Figure S6, see also the Materials and Methods).

Using this strategy, we analyzed caveolae in PRIME-PAINT images of U2OS cells labeled for caveolin-1 (Figure S7). WEKA model performance was validated with a DICE similarity coefficient of 84 ± 8%. For each cell, we quantitated the cell area, signal intensity (i.e., total numbers of KRas and Caveolin-1 localizations), and nanostructure size (i.e., the diameter of individual caveolae; Figure S7 and Figure 4A,B). The level of expression for mutant KRas was calculated as the net number of KRas localizations (after combining localizations that span multiple raw frames) per μm^2 image area. Collectively, 925 cells containing a total of ∼630,000 caveolae were segmented and analyzed.

The analysis revealed an interesting relationship between the caveolae size and KRas mutant expression. The number of caveolae per cell was significantly lower in KRas^{G12D}-positive cells compared with KRas^{G12D}-negative cells, confirming our initial observation. However, the total amount of caveolin-1 protein appears to not be affected by KRas^{G12D} expression, at least within the short term (48−72 h) Dox induction used in this study (Figure 4C). Importantly, at all KRas expression

https://doi.org/10.1021/cbmi.3c00060
Chem. Biomed. Imaging 2023, 1, 817−830

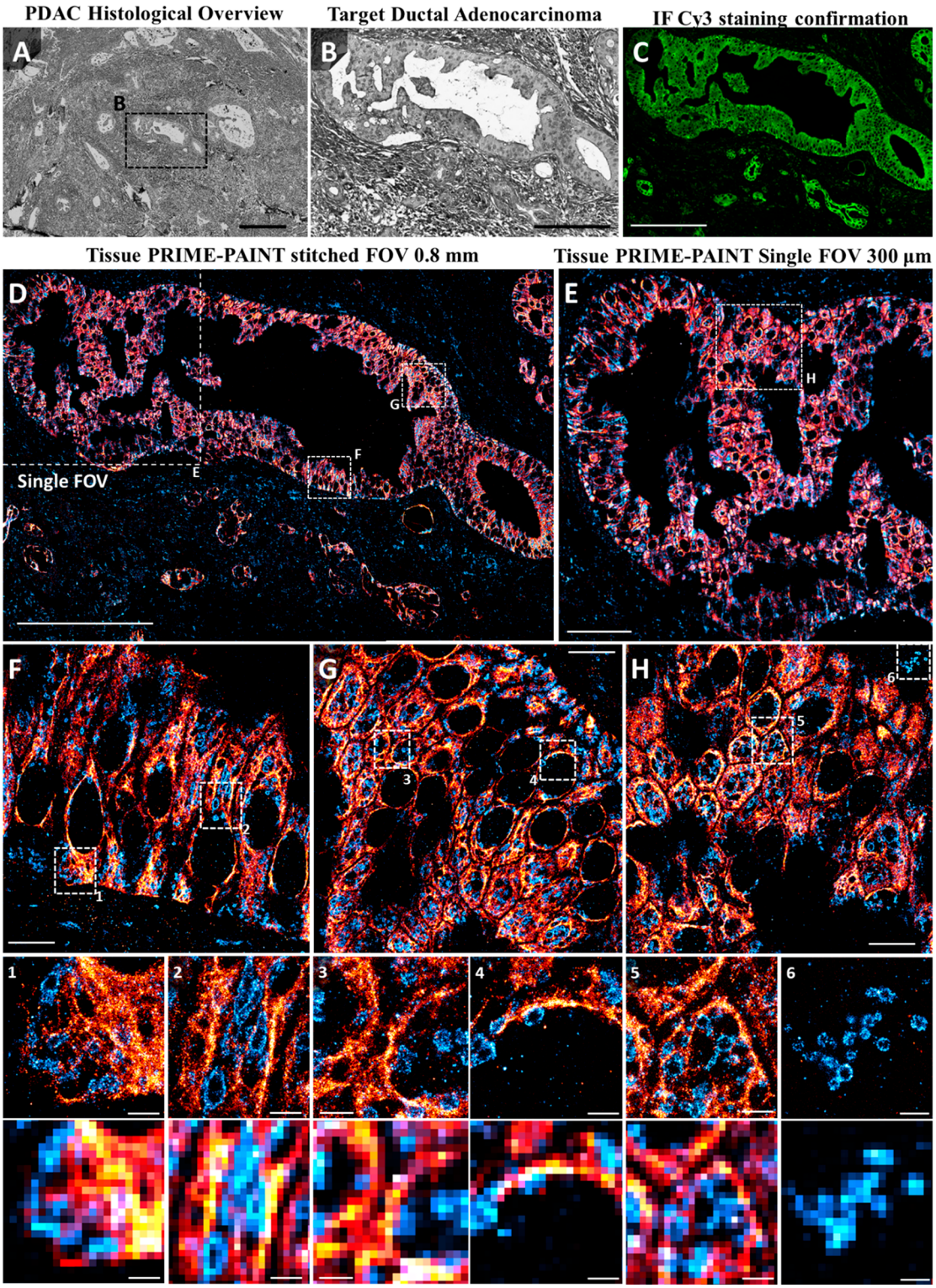

Figure 5. Multiplexed PRIME-PAINT of pancreatic cancer tissue. (A) Histological overview of moderately differentiated PDAC within desmoplastic stroma acquired at 20× magnification. (B) Targeted ductal adenocarcinoma for imaging with PRIME-PAINT. (C) Immunofluorescent confirmation of the Cy3 signal from secondary antibodies conjugated to docking strand oligos showing strong pan-cytokeratin staining along the tumor and diffuse mitochondrial labeling within the tumor and adjacent stroma. (D) Stitched tissue PRIME-PAINT image of an entire, 800 μm long ductal adenocarcinoma with both prognostic pan-cytokeratin in red and mitochondrial Tom20 in blue. (E) Single-FOV tissue PRIME-PAINT image obtained under mild flow ("microfluidics-enhanced"). (F−H) Select magnified regions from parts D and E highlighting the high quality imaging of cellular features seen within different regions of the tumor. Numbered insets shown with matching diffraction limited views (300 nm pixel size). Tissue PRIME-PAINT two-target images (D−H) were acquired in 6 h total (30,000 frames at 60 ms exposure for each target) using PRIME-PAINT at 1 μL/min flow and 500 pM IS1-ATTO643 and 7% EC and 500 pM IS2-ATTO643 and 7% EC for pan-cytokeratin and Tom20, respectively. Scale bars are 500 μm in part A, 200 μm in parts B−D, 50 μm in part E, 10 μm in parts F−H, and 2 μm for both PRIME-PAINT and diffraction-limited bottom numbered insets.

https://doi.org/10.1021/cbmi.3c00060
Chem. Biomed. Imaging 2023, 1, 817−830

levels examined (0−60+ localizations/μm^2), the histograms of caveolae diameter showed two distinct peaks at ∼54 and ∼154 nm (Figure 4D), which we tentatively attributed to fully formed caveolae (∼60 nm diameter) and precursor "plaques" (∼150 nm diameter) as previously identified in EM images.[34] As the level of $KRas^{G12D}$ expression increased, the peak diameters remained largely unchanged (Figure S8) but the fraction of large caveolae noticeably decreased (Figure 4D). This observation may support that active KRas promotes caveolae maturation, echoing previous reports,[35,36] although the effect may be cell-line and context specific.

While a full validation of this result and its mechanistic interpretation warrant a more extended study, this example demonstrates the feasibility in utilizing PRIME-PAINT in combination with machine-learning-based image segmentation in probing alterations in nanoscopic structures across large cell populations, which would have been difficult if not for both the nanoscale resolution and the larger FOVs.

Microfluidics-Enhanced DNA-PAINT Nanoscopy of Clinical FFPE Tissue Samples

Although FFPE tissue nanoscopy via STORM has been demonstrated for years,[17] reports demonstrating the same with DNA-PAINT have been lacking. The main motivations for imaging FFPE tissue sections with DNA-PAINT would be high spatial resolution, convenient multiplexing, and reliable stitching. In DNA-PAINT, photobleaching is limited to the fluorophore attached to the imaging strand oligonucleotide and does not affect the target-attached docking strand. As such, imaging of the current FOV has little impact on the neighboring sample areas (unlike STORM; Figure S9A−C), permitting robust stitching across as many FOVs as necessary to address even larger sample areas.

To our surprise, initial attempts of DNA-PAINT imaging on FFPE tissue sections yielded a much lower localization density compared to that on cells (Figure S9D,E) and, in consequence, poorly reconstructed images, despite efficient and on-target labeling as confirmed by examining the signals from Cy3 attached to the DS oligos. Considering the quality difference with previous tissue STORM results[17] prepared using nearly identical antigen retrieval and similar staining methods, we suspected that the lack of DNA-PAINT signals was due to inefficient DS-IS hybridization. Accidentally, we observed that the localization kinetics was drastically improved when the perfusing pump was left on during image acquisition (Figure S10A). Follow-up investigations showed that a weak flow at 1 μL/min could already increase the observed localizations by ∼10-fold and resulted in significantly better image quality (Figure S10B,C). No additional benefits were evident when the flow rate was increased to 5 μL/min. In contrast to imaging the tissue sections, microfluidic flow during imaging only situationally helped DNA-PAINT imaging of cells grown on glass, perhaps because the localization kinetics was already near optimal on cultured cells (Figure S11).

Several other empirical modifications to sample preparation and imaging steps helped further improve PRIME-PAINT imaging of FFPE tissue sections. First, we found that the optimal EC% for FFPE tissue sections is between 5 and 8% (for cells typically 10−15% EC) (Figure S12). This might be related to refractive index matching between the EC-containing buffer and the sample.[37] Second, addition of Signal Enhancer (SE), a charge-blocking commercial product previously used in our DNA-PAINT(-ERS) sample preparations,[19] followed by RNase A treatment during blocking prior to antibody incubations yields the best PRIME-PAINT images on FFPE sections (Figure S13).

Multiplexed Nanoscopy of Pancreatic Tumor Sections with PRIME-PAINT

We chose to use FFPE sections of Pancreatic Ductal Adenocarcinoma (PDAC) to exemplify multiplexed tissue nanoscopy with PRIME-PAINT. Dual labeling for Tom20 and pan-cytokeratin could inform structural changes in mitochondrial organization, which are theorized to occur during PDAC development.[38−41] To capture such structural changes with fine details, nanoscopic imaging of whole pre-PDAC and PDAC lesions—often hundreds of micrometers across—is necessary.

A histological overview photographed with a 20× objective revealed a moderately differentiated PDAC within desmoplastic stroma (Figure 5A and B). Using signals from Cy3-DS conjugated to the secondary antibodies as a reference, immunofluorescence confirmed strong pan-cytokeratin staining along the duct and faint mitochondria in and around the duct (Figure 5C). By acquiring six adjacent FOVs with PRIME-PAINT at ∼0.3 mm × 0.3 mm each with a 40 μm overlap, we imaged the entire duct and proximal stroma covering an area of over 800 μm × 500 μm (Figure 5D). At an acquisition speed of 30 min per FOV per target, the entire imaging took ∼3 h for each target and ∼6 h for a dual-target image.

Close-up views demonstrate uniform image quality over the entire FOV (Figure 5E). In smaller ROIs, sub-diffractive details of mitochondria and pan-keratin can be seen in unparalleled detail versus an otherwise diffraction limited blur (Figure 5F−H and insets 1−6). Not only can distinct mitochondria of varying sizes and shapes be seen, but dense pan-cytokeratin also tapers to fine, filamentous networks, often enclosing the cell periphery. Finally, to further exemplify the full range of spatial information obtainable by PRIME-PAINT on FFPE tissue sections, we serially magnified a second ductal adenocarcinoma from the millimeter-scale overview down to distinct mitochondrial membrane structures (Figure S14). Based on this multiscale view of entire tissue regions, we should be able to quantitatively compare the structure and spatial organization of mitochondria and the intermediate cytoskeleton in different types of cells within the same tissue as well as in tissues from different origins (such as lesions at different stages of PDAC).

■ CONCLUSION AND DISCUSSIONS

We have demonstrated PRIME-PAINT, a new platform for multiplexed bioimaging across roughly 5 orders of length scales (∼10 nm to mm scales). PRIME-PAINT is based on a simple optical design and capitalizes on improvements in imaging kinetics, sample preparation, and microfluidics for fast and high-quality biological nanoscopy of broad sample types.

Although several solutions are already available for large-field biological nanoscopy, PRIME-PAINT has some unique advantages. PRIME-PAINT affords among the largest single imaging FOVs (∼0.5 mm × 0.5 mm) of all fluorescence nanoscopies, comparable to that of chip-based nanoscopy. It also offers among the best lateral resolutions at the full FOV (40−45 nm), while even at the smaller FOV, ∼0.3 mm × 0.3 mm, the latter resolution (25−30 nm) is comparable to previous nanoscopy modalities with through-objective imaging

https://doi.org/10.1021/cbmi.3c00060
Chem. Biomed. Imaging 2023, 1, 817−830

schemes with smaller FOVs. Owing to the accelerated imaging kinetics with DNA-PAINT-ERS,[19,20] PRIME-PAINT allows imaging of millimeter-scale sample regions in as little as 40 min per target. Lastly, PRIME-PAINT is built on DNA-PAINT and thus naturally excels at multiplexed imaging, especially with the integrated microfluidic sample chamber. These traits make PRIME-PAINT ideally suited for studying complex biological systems/interactions that require multiscale and multicomponent imaging capabilities.

The prism-illumination scheme has been widely used in single-molecule imaging studies. The imaging setup reported in this work, which is slightly modified from the original prism-type TIR, comprises only off-the-shelf components and can be readily adopted without needing sophisticated scanning optics[10] or microfabricated imaging substrates.[12] The integrated microfluidic imaging chamber can also be constructed using only commercial parts, although a custom, machined chamber holder is encouraged for improved mechanical stability and reliability. As such, PRIME-PAINT can be constructed and maintained for routine operations in most biological laboratory settings.

PRIME-PAINT can be improved and extended in several aspects. The spatial resolution of PRIME-PAINT was primarily limited by the excitation power density and could be further improved with simple solutions such as using a more powerful laser or combining with other illumination schemes such as ASTER[10] (line-scanning) or "flat-top" beam shaping[42] (wide-field). The latter two schemes also create homogeneous illumination across the FOV for more uniform imaging than the Gaussian beam used in this work. Image quality can also be improved by correcting for optical aberrations, which, even with optimized optics and light paths, cannot be neglected given the large FOVs.[29,30,43] Such aberrations also pose challenges when stitching images from multiple FOVs.[28] Aside from these potential improvements, PRIME-PAINT is by design amenable to automation through integration of programmable fluidics, FOV stitching and buffer exchange,[44] and online data processing.[45,46] Leveraging recent progress in multiplexing strategies[47−49] and 3D calibration over extended depth and large FOVs,[43,50] 3D PRIME-PAINT imaging of many more targets over several mm^2 sample areas should be readily feasible.

By significantly extending the imaging throughput of fluorescence nanoscopy, PRIME-PAINT and the other recent, large-FOV modalities[9−12] bring exciting new opportunities. Similar to cryo-EM single-particle analysis, which revolutionized structural biology, recent work has used nanoscopy data to infer dynamic protein complexes.[51,52] Large-scale nanoscopic image data sets will synergize with machine-learning-based image analysis tools such as WEKA[32] and LocMoFit[53] to significantly accelerate biomedical discovery.[54,55] Additionally, the ability to image FFPE sections at nanometer resolution across mm^2 FOVs (Figure 5 and Figure S14) is an important step toward clinical applications, for which PRIME-PAINT and the likes represent a leap forward compared with prior attempts using electron microscopy (EM)[56−58] or fluorescence nanoscopy with a small FOV.[16,17]

MATERIALS AND METHODS

Materials

Methods utilized for generating labeling reagents followed established protocols for DNA-PAINT-ERS.[19] In brief, all starting DNA oligonucleotides were obtained from Integrated DNA Technologies. Docking strands included a 5′ amino modifier C6, for further conjugation with DBCO-PEG4-NHS (Click Chemistry Tools, A134-2) via succinimidyl ester chemistry, and a 3′ Cy3 fluorophore which helps confirm proper antibody labeling. Imaging strands with a 3′ amino group were reacted using succinimidyl ester chemistry with NHS-ATTO 643 (ATTO-TEC, AD 643-31). All reactions were performed at room temperature in ultrapure water adjusted to pH ∼8.5 using 1 M sodium bicarbonate (Fisher Scientific, M-14636) for 3 h. Conjugated DNA oligos were purified via ethanol precipitation and resuspended in Invitrogen UltraPure DNase/RNase-Free Distilled water (Thermo Fisher Scientific, 10977023).

The secondary antibodies used were AffiniPure Donkey anti-Rabbit IgG (H+L) (Jackson Immuno Research 711-005-152), AffiniPure Donkey anti-Mouse IgG (H+L) (Jackson Immuno Research 715-005-150), and AffiniPure Donkey anti-Chicken IgG (H+L) (Jackson Immuno Research 703-005-155); these were conjugated with azido-PEG4-NHS via succinimidyl ester chemistry. Antibody-PEG4-azide conjugates were purified through a 50 kDa Millipore Sigma Amicon Ultra Centrifugal Filter Unit (Fisher Scientific, UFC505096). Next, purified antibody-PEG4-azide was reacted with excess DBCO-DS (molar ratio 1:5) via copper-free click chemistry, overnight at room temperature using a rocker. Antibody-DS products were isolated through a 100 kDa Millipore Sigma Amicon Ultra Centrifugal Filter Unit (Fisher Scientific, UFC510096). Protein concentrations and the degrees of labeling were found using the peak signals at 260, 280, and 550 nm (for Cy3TM) in a Nanodrop UV−vis spectrophotometer (ThermoFisher Scientific, 2000c). In general, the oligo-conjugated secondary antibodies generated contained 4−5 conjugated DS oligos.

The SNAP-tag substrate BG-PEG4-azide was synthesized by the Medicinal Chemistry Core at OHSU. Briefly, it was synthesized in two steps via an amine-reactive key intermediate prepared from commercially available BG-NH2 as the starting material, followed by an NHS-ester cross-linking reaction. The final crude product was purified by preparative HPLC. The structure and purity of BG-PEG4-azide were further confirmed by analytical HPLC and high-resolution mass spectrometry prior to click oligonucleotide labeling. BG-PEG4-azide was reacted with excess DBCO-DS (molar ratio 10:1) via copper-free click chemistry on a rocker at room temperature overnight. The resulting BG-DS was purified via ethanol precipitation and suspended in UltraPure DNase/RNase-Free Distilled water. The concentration was determined by a Nanodrop UV−vis spectrophotometer, similarly to that mentioned above.

The primary antibodies used were Mouse-beta tubulin monoclonal antibody (Thermo Fisher Scientific, 32-2600), Rabbit-anti-Tom20 polyclonal antibody (Abcam, ab78547), Rabbit-anticaveolin-1 antibody (Abcam, ab2910), Chicken-antivimentin antibody (Sigma-Aldrich, AB5733), and Mouse panCytokeratin (Abcam, ab7753).

For all remaining experimental steps and sample processing and labeling (fixation, permeabilization, immunostaining, etc.), the materials used included paraformaldehyde (Sigma-Aldrich, P6148), Triton X-100 (Sigma-Aldrich, X100), 25% glutaraldehyde (Sigma-Aldrich, G6257), bovine serum albumin (Fisher Scientific, BP1600), sodium hydroxide (Fisher Scientific, S318-100), sodium borohydride (Sigma-Aldrich, 452882), Invitrogen Salmon Sperm DNA (Thermo Fisher Scientific, AM9680), sodium azide (Fisher Scientific, AC190381000), Gibco Dulbecco's PBS with calcium and magnesium (PBS+) (Thermo Fisher Scientific, 14-040-182), and 50 nm gold particles (BBI Solutions, EM.GC50/4). Fixation was performed using a buffer made from 2× PHEM buffer, generated with 0.06 M PIPES (Sigma-Aldrich, P6757), 0.025 M HEPES (Fisher Scientific, BP310-500), 0.01 M EGTA (Thermo Fisher Scientific, O2783-100), and 0.008 M $MgSO_4$ (Acros, 4138-5000) in distilled water, and 10 M potassium hydroxide (Sigma-Aldrich, 221473) was used to finally adjust the pH to 7. As with DNA-PAINT-ERS, a % volume combination of EC (Sigma-Aldrich, 676802) with buffer C (PBS plus 500 mM sodium chloride) was used as indicated for both imaging and washing steps.

https://doi.org/10.1021/cbmi.3c00060
Chem. Biomed. Imaging 2023, 1, 817−830

Flow-Chamber Preparation and Cell Culture

Flow chamber substrates were made using 25 × 75 mm^2 fire-polished microscope slides (Schott, Nexterion Slide Glass B 1025087). Fire-polished microscope slides were each drilled twice using a 1/16th inch bit diamond coated drill bit (Lasco Diamond #F6) for later use as microfluidic inlet and outlet ports, at the coordinates of (4 mm, 16 mm) and (21 mm, 59 mm) on the 25 × 75 mm^2 coverslide. After drilling, slides were rinsed with DI water (3×) and sonicated in 100% EtOH for 10 min. Following 3× DI water rinses, slides were etched in 1 M NaOH for 20 min. After three rinses with DI water, cleaned slides were left in 100% EtOH prior to cell culture and tissue slide preparation.

Cell and Tissue Samples

Cell lines used in this study included U2OS (ATCC, HTB-96) and COS7 (ATCC CRL-1651). U2OS and Cos7 cells were passaged every 3−4 and 2−3 days, respectively, and cultured in Gibco DMEM (Thermo Fisher Scientific, 11995073) mixed with 10% fetal bovine serum (Thermo Fisher Scientific, 26-140-079). Passaging was performed using Trypsin-EDTA (0.25%) (Thermo Fisher Scientific 25200056), with cells kept to below 15 passages. For SRM imaging experiments, cells were grown on custom drilled coverslides within a sterile oval silicon cutout until 50−60% confluency was reached prior to fixation.

All patient FFPE tissue samples (including HER2+ breast cancer and PDAC samples) were collected through either the OHSU Biorepository or the Brenden Colson Center following IRB approved protocols, including patient consent for research applications. Standard human pancreas samples obtained by BCC were FFPE sections from otherwise healthy cadavers and were used for most tissue imaging optimizations. FFPE tissue samples were cut using an ultramicrotome in 2 πm thick sections (RM2125 RTS, Leica Biosystems, Germany).

Predrilled and cleaned fire-polished coverslides were prepared for tissue mounting using a polyethylene-imine (PEI) (Sigma-Aldrich, 904759-100G) coating. In brief, cleaned coverslides were treated for 20 min with 0.1% PEI solution in ultrapure H_2O. After coating, excess PEI was rinsed 3× with ultrapure H_2O for 5 min each. After aspirating excess H_2O, coated slides were left to dry flat at 42 °C for 2+ h or until completely dried. Fluidic chamber profile outlines were drawn onto the non-PEI-coated backside by using an ultrafine sharpie to assist in tissue mounting positioning. All tissue samples were sectioned at 2 ±0.5 μm thickness and floated on a 42 °C water bath immediately prior to mounting onto PEI-coated coverslides. Mounted tissue sections were dried vertically for 1 h at 60 °C before storage. Mounted tissue sections were stored vertically in this manner for up to 1 month prior to antigen retrieval, labeling, and imaging.

Immunostaining

For immunostaining of caveolin and SNAP, cells were fixed for 20 min with 3.7% paraformaldehyde (PFA) in 1× PHEM buffer after a quick PBS wash. Following two PBS washes, cells were quenched with fresh 0.1% sodium borohydride in PBS for 7 min and followed by three washes with PBS (5 min each). Cells were permeabilized with 0.3% saponin in PBS for 20 min. For immunostaining of microtubules, Tom20 and vimentin, cells were fixed for 20 min with 3.7% PFA and 0.1% glutaraldehyde (GA) in 1× PHEM, followed by 3× PBS washes, quenching with sodium borohydride, and permeabilization in 0.2% Triton X-100 in PBS. Blocking in PBS with 3% bovine serum albumin and 5% salmon sperm DNA (Thermo Fisher Scientific, AM9680) for 45 min was done on a rocker, followed by incubation with the primary antibody for Tom20 (1:250), caveolin (1:200), tubulin (1:100), or vimentin (1:250) antibodies in PBS buffer containing 3% BSA. The incubation took place overnight on a rocker at 4 °C in a humidity chamber. Next, cells were washed three times (5 min each) with PBS before incubation with respective secondary antibody-DS described above at a final concentration of ∼8 μg mL^{-1} in PBS buffer containing 1% BSA and 5% salmon sperm DNA; the secondary antibody incubation also took place on a rocker at room temperature for 90 min. For DS secondary antibody incubation and subsequent steps, the sample was kept in the dark to avoid the bleaching of conjugated fluorophores. Cells were washed three times with PBS (5 min each). All cell samples were postfixed for 10 min with 3.7% PFA and 0.1% GA in 1× PHEM. Before imaging, cells were incubated with 15% 50 nm gold particles in PBS+ for 1 min, followed by a quick PBS wash.

For immunostaining of FFPE tissue samples, FFPE sections were deparaffinized using xylene (2×, 10 min), 100% EtOH (2×, 10 min), 95% EtOH in DI water (5 min), 70% EtOH in DI water (5 min), and 50% EtOH in DI water (5 min) and left in PBS. Tissues underwent antigen retrieval in a decloaking chamber (Bio SB, BSB-7087) first in Tris buffer (300 mM Tris, 0.05% Tween 20, pH 8). Tissues were transferred into a preheated citrate buffer (300 mM NaCitrate Monohydrate, 0.05% Tween 20, pH 6), also heated during decloaking, and allowed to cool to room temperature. After two PBS washes, tissues were further permeabilized with 0.4% Triton X-100 in PBS for 45 min. After the excess permeabilization solution and three PBS washes were removed, a hydrophobic barrier (company product) was applied around the mounted tissue following the fluidic outline of the chamber design. Tissues were either further treated with RNase A/Image-iT FX signal enhancer (ThermoFisher Scientific, I36933) or directly blocked prior to antibody labeling. In brief, RNase A and signal enhancer treatment both occurred prior to antibody labeling as optional optimizations. After permeabilization, tissue samples could be treated with RNase A (ThermoFisher Scientific, EN0531) at 50× dilution in PBS on a rocker overnight at room temperature. After a rinse with PBS, sections were quenched with fresh 0.1% sodium borohydride in PBS for 7 min, followed by three washes with PBS (5 min/each). Tissue was further incubated with signal enhancer at room temperature for 30 min, followed by three washes with PBS (5 min/each).

After PBS washes, tissues were blocked with 3% BSA and 0.3% saponin in PBS for 1 h. Next, the tissues were incubated with primary antibodies: Tom20 (1:200 dilution) and pan-Cytokeratin (1:150 dilution) in PBS containing 3% BSA and 5% salmon sperm DNA. The incubation took place on a rocker overnight at 4 °C in a humidity chamber. Following three PBS washes (5 min each), tissues were incubated with respective DS-conjugated secondary antibodies at a final concentration of ∼8 μg mL^{-1} in PBS buffer containing 1% BSA and 5% salmon sperm DNA. The incubation also took place on a rocker at room temperature for 2 h, followed by three PBS washes (5 min each). After this, all tissue samples were postfixed by 3.7% PFA and 0.1% GA in 1× PHEM at room temperature for 30 min. Before flow chamber assembly, tissues were incubated with 15% 50 nm gold particles in PBS+ for 1 min followed by a quick PBS wash.

Flow Chamber Assembly

The flow chamber exterior was made using a CNC-cut aluminum holder which fits gently outside the sample sandwich, providing compression to meet matching 1/16 fractional width O-rings (McMaster-Carr, 2418T11) and Tygon tubing (Cole-Parmer, EW-06419-01) at the predrilled points on the coverslide. This external holder and microfluidic tubing can be easily reused for each sample (see the CAD file in the Supporting Information). Since the sample coverslide still provides the backbone of the fully assembled sample and fluidics for imaging, both the microscope objective and prism can be used at nearly identical positions between samples.

To complete flow chamber interior assembly around immunolabeled cells/tissues mounted to predrilled coverslides, 24 mm × 40 mm high-precision #1.5 coverslips (Thorlabs, CG15KH) and 2 in. wide Behmis Parafilm (Thermo Fisher, 12-374-16) were first combined. After sonicating coverslips in 100% EtOH for 10 min, coverslips were quickly air-dried using a gentle stream of compressed air. Parafilm was cut into 1 in. wide sections and stretched lengthwise until just prior to tearing. Stretched Parafilm was placed onto coverslips such that no folds or airpockets were present. Excess Parafilm was removed from the coverslip border using a razorblade, and a fluid profile stencil was used to cut the flow chamber interior into the parafilm. After the inner part of the Parafilm was peeled off, the coverslip and fluidic profile were ready for final assembly. After

https://doi.org/10.1021/cbmi.3c00060
Chem. Biomed. Imaging 2023, 1, 817−830

excess PBS was removed from cells/tissues, coverslips with fluidic profiles were slowly placed on top of the coverslide with sample such that no excess solution contacted the Parafilm border. A 110 W glue gun tip (with glue removed) was used to gently press the coverslip along the Parafilm border to melt the Parafilm and seal the fluidic chamber.

The fluidic components used were an MX Series II 10 Position/11 Port Selector Valve (IDEX Health & Science, MXX778-605) and an RP-TX Peristaltic Pump (Takasago Electric, RP-TXP5S-P04A-DC3VS). Pump control was achieved through Arduino Uno (Amazon, X7375-10G) and Adafruit Motor/Stepper/Servo Shield for Arduino v2 Kit (Adafruit, 8541582581). Both the port selector and peristaltic pump were controlled via custom C code.

Microscopy

Through-objective TIRF super-resolution data in this work were taken on a custom single-molecule imaging system described previously.[19] Briefly, two lasers emitting at 561 nm (Opto Engine LLC, 150 mW) and 647 nm (Coherent OBIS 647, 140 mW) were combined and introduced into the back of a Nikon Ti−U microscope equipped with a 60× TIRF objective (Nikon, oil immersion, NA 1.49). An f = 400 mm lens was placed at the back port of the microscope to focus the collimated laser light to the back aperture of the objective to achieve objective TIR illumination. The excitation light can be continuously tuned between epi-fluorescence and strict TIR angle modes by shifting the incident laser horizontally with a translational stage before entering the back port of the microscope. Additionally, a weak cylindrical lens compensates for longitudinal beam widening through the prism to maintain power density over a round FOV for efficient single-molecule excitation. A custom focus stabilizing system based on the detection of the reflected excitation laser was used to stabilize the focus during data acquisition. A multiedge polychroic mirror (Semrock, Di01-R405/488/561/635) was used to reflect the lasers into the objective and clean up fluorescence signals from the sample. The emission filters used for the 561 nm (for imaging Cy3 on the DS) and 647 nm (for imaging ATTO643 conjugated ISs) were FF01-605/64 and FF01-708/75, respectively (all from Semrock). Fluorescence signals were collected through the objective by an electron-multiplied charge-coupled device (EM-CCD, Andor, iXon Ultra 897) using a typical EM gain setting at 200−300 in frame transfer mode. Unless otherwise indicated, the power density of the 647 nm laser (for DNA-PAINT imaging using ATTO643 conjugated IS) was typically ∼500 W/cm^2.

Prism-type TIRF PRIME-PAINT data was collected using a custom single-molecule imaging system as outlined in Figure 1A. Key system components used from the laser to the camera were as follows: 1 W 639 nm laser (Opto Engine, MRL-FN-639-1W), 2× beam expander (ThorLabs BE02M-A), cylindrical lens f = 1000 mm, 5× beam expander (ThorLabs GBE05-A), 2−5× continuous beam expander (ThorLabs BE02-05-A), 4π lens cage (using an f = 100 mm and an f = 80 mm lens), 10 mm Square Aperture UV Fused Silica Prism (Pellin Broca, ADBU-10), 40× silicon oil objective (Nikon, Plan APO 40×/1.25 Sil λS WD 0.3, MRD73400), 647 nm long pass filter (Semrock, LP02-647RU-50), 633 nm Stopline notch filter (Semrock NFD01-633-25 × 36), and finally either a side-mounted Prime-95B sCMOS (Teledyne Photometrics, Prime 95B 25MM) or Kinetix sCMOS (Teledyne Photometrics). All detection path components were housed within a Nikon Eclipse Ti2-E microscope body. Perfect Focus Unit (Nikon PFS, TI2-N-NDA-P) was integrated into the microscope body and provided stable autofocusing even during mild flow integration during PRIME-PAINT imaging.

Data Acquisition and Image Processing

Super-resolution images were acquired using the open source micromanager software suite (https://micro-manager.org/)[59] and saved as OMERO TIF files. Image analyses for extracting single-molecule localization and subsequent localization filtering, sorting, and rendering were performed using in-house Matlab scripts.[60] Briefly, raw localizations were first filtered based on localization fitting parameters such as signal-to-noise ratio, widths of point spread functions in the x and y dimensions, aspect ratio, etc. Next, the localizations were sorted, during which events that appeared within a defined number of frames (typically 2−3) and distance (typically 80 nm) were combined into a single event with averaged coordinates. The sorted localizations were then used for final image rendering, and the rendered images were saved as TIF files for further analysis and annotations in Fiji. Multicolor images were co-registered using an average of observed gold fiducial positions within each FOV.

Multi-FOV image stitching was done by using matched fibers between adjacent FOVs. Typically, adjacent FOVs have a 25−50 μm overlapping region. All fiducials in the overlapping regions are located and assigned to matching pairs, and the average pixel shifts in both lateral dimensions are determined based on the distance calculations between all matching pairs. A coordinate shift is then applied to the moving image to yield an aligned image with the static image; no other image transformations are performed at present. Of note, this method does not yield stitching with sub-diffractive registration precisions due to the presence of optical aberrations at the FOV periphery, and an optimal solution that integrates aberration correction and nanoscale stitching is being developed.

Custom Machine-Learning Integrated Fiji Macro

Our analysis was built using the Fiji macro language in .ijm format. Machine learning segmentation/classification was performed using the Trainable WEKA Segmentation plugin within Fiji.[32] Training was performed using input images with manually drawn caveolae particle boundaries trained against background diffuse cytoplasmic caveolin-1. Subsequent testing of trained model performance against manually annotated caveolae on three additional data sets resulted in a DICE coefficient of 84 ± 8%.

The macro workflow is visually shown in Figure S6. This begins by opening a multitarget PRIME-PAINT rendered image, typically 29,100 × 29,100 pixels, and using Fiji ROI manager to manually draw boundaries for each cell of interest to quantify. After initiation, the full PRIME-PAINT image is loaded into the WEKA plugin and the trained.model file for caveolae is loaded, with all subsequent steps happening automatically. For each picked cell ROI, the macro will cut the cell out of the full PRIME-PAINT image, masking the signal outside the ROI, and automatically generate subimages with an adjustable overlap to tile across each cell ROI analyzed. Each subimage is temporarily saved, and WEKA classification is performed on each cell's subimage. After classifying each subimage of a particular cell, dynamic offsets initially added during subimage generation are removed and the full classified cell is combined using original coordinates. The distinct ROIs for all detected vesicles are saved and used to measure original cell image attributes at the positions indicated from WEKA classification outputs. In practice, our custom Fiji macro would automatically segment caveolae from input cells at a rate of ∼30 min per cell, although this performance will vary depending on the computer specifications used. These per-cell caveolae measurements are saved as .csv outputs and can be postprocessed using programs such as R.

Population Analysis and Other Plots

Outside the rendered images, all plots were generated in R using the ggplot package. Caveolae particles smaller than 20 nm were excluded from downstream analysis, as their border could not be reliably determined and they were not considered as a part of the initial manual annotation for observed caveolae particles. Population analysis was performed using the nls() function in R, which was used to model a two-Gaussian population within the total observed populations of caveolae particle sizes according to diameter.

Statistical Analysis

Image analysis was performed using a custom semiautomated machine learning macro installed in ImageJ (see Figures S7 and S8). DNA-PAINT images with manually annotated cell boundary .roi were input to extract caveolae particle positions as .roi lists. Mapping these per-caveolae particle .roi positions onto the original image, the ImageJ "Measure" function was used to extract and save .csv files per cell, with image attributes including area, diameter, mean intensity, etc. All downstream analysis and visualization was performed in R.

https://doi.org/10.1021/cbmi.3c00060
Chem. Biomed. Imaging 2023, 1, 817−830

The *P*-value calculations in Figure 4C were performed using the Wilcoxon test in the stat_compare_means() function within the ggplot package in R. For Figure 4D, the *Y* axis of size population prevalence was calculated using the geom_density function in ggplot from the $\log_{10}$-transformed *X* axis of all caveolae particle diameters.

■ ASSOCIATED CONTENT

Supporting Information

The Supporting Information is available free of charge at https://pubs.acs.org/doi/10.1021/cbmi.3c00060.

Supplementary Figures S1−14; additional illustrations on the PRIME-PAINT setup, performance, data analysis workflows, sample preparation optimizations, and example images (PDF)

CAD files for the custom parts in the fluidic holder design (ZIP)

■ AUTHOR INFORMATION

Corresponding Author

Xiaolin Nan − *Cancer Early Detection Advanced Research Center, Knight Cancer Institute, Oregon Health & Science University, Portland, Oregon 97201, United States; Program in Quantitative and Systems Biology, Department of Biomedical Engineering, Oregon Health & Science University, Portland, Oregon 97201, United States;* orcid.org/0000-0002-0597-0255; Email: nan@ohsu.edu

Authors

Matthew J. Rames − *Cancer Early Detection Advanced Research Center, Knight Cancer Institute, Oregon Health & Science University, Portland, Oregon 97201, United States; Program in Quantitative and Systems Biology, Department of Biomedical Engineering, Oregon Health & Science University, Portland, Oregon 97201, United States*

John P. Kenison − *Cancer Early Detection Advanced Research Center, Knight Cancer Institute, Oregon Health & Science University, Portland, Oregon 97201, United States;* orcid.org/0000-0003-4138-6600

Daniel Heineck − *Cancer Early Detection Advanced Research Center, Knight Cancer Institute, Oregon Health & Science University, Portland, Oregon 97201, United States; Program in Quantitative and Systems Biology, Department of Biomedical Engineering, Oregon Health & Science University, Portland, Oregon 97201, United States*

Fehmi Civitci − *Cancer Early Detection Advanced Research Center, Knight Cancer Institute, Oregon Health & Science University, Portland, Oregon 97201, United States*

Malwina Szczepaniak − *Program in Quantitative and Systems Biology, Department of Biomedical Engineering, Oregon Health & Science University, Portland, Oregon 97201, United States;* orcid.org/0000-0002-1230-9190

Ting Zheng − *Cancer Early Detection Advanced Research Center, Knight Cancer Institute, Oregon Health & Science University, Portland, Oregon 97201, United States*

Julia Shangguan − *Program in Quantitative and Systems Biology, Department of Biomedical Engineering, Oregon Health & Science University, Portland, Oregon 97201, United States*

Yujia Zhang − *Cancer Early Detection Advanced Research Center, Knight Cancer Institute, Oregon Health & Science University, Portland, Oregon 97201, United States; Program in Quantitative and Systems Biology, Department of Biomedical Engineering, Oregon Health & Science University, Portland, Oregon 97201, United States*

Kai Tao − *Program in Quantitative and Systems Biology, Department of Biomedical Engineering, Oregon Health & Science University, Portland, Oregon 97201, United States*

Sadik Esener − *Cancer Early Detection Advanced Research Center, Knight Cancer Institute, Oregon Health & Science University, Portland, Oregon 97201, United States; Program in Quantitative and Systems Biology, Department of Biomedical Engineering, Oregon Health & Science University, Portland, Oregon 97201, United States*

Complete contact information is available at: https://pubs.acs.org/10.1021/cbmi.3c00060

Author Contributions

J.P.K. and D.H. contributed equally to this work. Conceptualization: X.N., F.C., M.J.R.; Methodology: M.J.R., X.N., J.P.K., D.H., T.Z., M.S., J.S.; Investigation: M.J.R., J.P.K., D.H., Y.Z., T.Z., K.T.; Visualization: M.J.R., J.P.K., Y.Z.; Supervision: X.N., S.E.; Writing—original draft: M.J.R., X.N.; Writing—review and editing: M.J.R., X.N., M.S., T.Z., Y.Z., K.T., S.E.

Notes

The authors declare no competing financial interest.

■ ACKNOWLEDGMENTS

The authors thank Drs. Joe W. Gray, Gordon Mills, Terry K. Morgan, Young Hwan Chang, Jason Link, Sean Speese, Yu-Jui (Roger) Chiu, David Qian, and many other colleagues at OHSU for their helpful discussions. M.J.R., F.C., J.P.K., D.H., T.Z., Y.Z., S.E., and X.N. are members of and supported by the Cancer Early Detection Advanced Research (CEDAR) Center of the OHSU Knight Cancer Institute. The work is supported in part by the OHSU Knight Cancer Institute, the Damon Runyon Cancer Research Foundation, the Cancer Systems Biology Consortium from the National Cancer Institute (CSBC, grant number U54 CA209988, PI: Joe W. Gray), and the National Institute of General Medical Sciences (grant number R01 GM132322, PI: X.N.).

■ REFERENCES

(1) Betzig, E.; Patterson, G. H.; Sougrat, R.; Lindwasser, O. W.; Olenych, S.; Bonifacino, J. S.; Davidson, M. W.; Lippincott-Schwartz, J.; Hess, H. F. Imaging Intracellular Fluorescent Proteins at Nanometer Resolution. *Science* **2006**, *313* (5793), 1642−1645.

(2) Hess, S. T.; Girirajan, T. P. K.; Mason, M. D. Ultra-High Resolution Imaging by Fluorescence Photoactivation Localization Microscopy. *Biophys. J.* **2006**, *91* (11), 4258−4272.

(3) Rust, M. J.; Bates, M.; Zhuang, X. Sub-Diffraction-Limit Imaging by Stochastic Optical Reconstruction Microscopy (STORM). *Nat. Methods* **2006**, *3* (10), 793−795.

(4) Sharonov, A.; Hochstrasser, R. M. Wide-Field Subdiffraction Imaging by Accumulated Binding of Diffusing Probes. *Proc. Natl. Acad. Sci. U. S. A.* **2006**, *103* (50), 18911−18916.

(5) Jungmann, R.; Avendaño, M. S.; Woehrstein, J. B.; Dai, M.; Shih, W. M.; Yin, P. Multiplexed 3D Cellular Super-Resolution Imaging with DNA-PAINT and Exchange-PAINT. *Nat. Methods* **2014**, *11* (3), 313−318.

(6) Hein, B.; Willig, K. I.; Hell, S. W. Stimulated Emission Depletion (STED) Nanoscopy of a Fluorescent Protein-Labeled Organelle inside a Living Cell. *Proc. Natl. Acad. Sci. U. S. A.* **2008**, *105* (38), 14271−14276.

(7) Balzarotti, F.; Eilers, Y.; Gwosch, K. C.; Gynnå, A. H.; Westphal, V.; Stefani, F. D.; Elf, J.; Hell, S. W. Nanometer Resolution Imaging

and Tracking of Fluorescent Molecules with Minimal Photon Fluxes. *Science* **2017**, *355* (6325), 606−612.
(8) Ostersehlt, L. M.; Jans, D. C.; Wittek, A.; Keller-Findeisen, J.; Inamdar, K.; Sahl, S. J.; Hell, S. W.; Jakobs, S. DNA-PAINT MINFLUX Nanoscopy. *Nat. Methods* **2022**, *19*, 1072.
(9) Zhao, Z.; Xin, B.; Li, L.; Huang, Z. L. High-Power Homogeneous Illumination for Super-Resolution Localization Microscopy with Large Field-of-View. *Opt Express* **2017**, *25* (12), 13382−13395.
(10) Mau, A.; Friedl, K.; Leterrier, C.; Bourg, N.; Lévêque-Fort, S. Fast Widefield Scan Provides Tunable and Uniform Illumination Optimizing Super-Resolution Microscopy on Large Fields. *Nat. Commun.* **2021**, *12* (1), 3077.
(11) Archetti, A.; Glushkov, E.; Sieben, C.; Stroganov, A.; Radenovic, A.; Manley, S. Waveguide-PAINT Offers an Open Platform for Large Field-of-View Super-Resolution Imaging. *Nat. Commun.* **2019**, *10* (1), 1267.
(12) Diekmann, R.; Helle, Ø. I.; Øie, C. I.; McCourt, P.; Huser, T. R.; Schüttpelz, M.; Ahluwalia, B. S. Chip-Based Wide Field-of-View Nanoscopy. *Nat. Photonics* **2017**, *11* (5), 322−328.
(13) Helle, Ø. I.; Coucheron, D. A.; Tinguely, J.-C.; Øie, C. I.; Ahluwalia, B. S. Nanoscopy On-a-Chip: Super-Resolution Imaging on the Millimeter Scale. *Opt. Express* **2019**, *27* (5), 6700−6710.
(14) Engdahl, A. K.; Belle, S.; Wang, T.-C.; Hellmann, R.; Huser, T.; Schüttpelz, M. Large Field-of-View Super-Resolution Optical Microscopy Based on Planar Polymer Waveguides. *ACS Photonics* **2021**, *8* (7), 1944−1950.
(15) Villegas-Hernández, L. E.; Dubey, V.; Nystad, M.; Tinguely, J.-C.; Coucheron, D. A.; Dullo, F. T.; Priyadarshi, A.; Acuña, S.; Ahmad, A.; Mateos, J. M.; Barmettler, G.; Ziegler, U.; Birgisdottir, Å. B.; Hovd, A.-M. K.; Fenton, K. A.; Acharya, G.; Agarwal, K.; Ahluwalia, B. S. Chip-Based Multimodal Super-Resolution Microscopy for Histological Investigations of Cryopreserved Tissue Sections. *Light Sci. Appl.* **2022**, *11* (1), 43.
(16) Xu, J.; Ma, H.; Ma, H.; Jiang, W.; Mela, C. A.; Duan, M.; Zhao, S.; Gao, C.; Hahm, E. R.; Lardo, S. M.; Troy, K.; Sun, M.; Pai, R.; Stolz, D. B.; Zhang, L.; Singh, S.; Brand, R. E.; Hartman, D. J.; Hu, J.; Hainer, S. J.; Liu, Y. Super-Resolution Imaging Reveals the Evolution of Higher-Order Chromatin Folding in Early Carcinogenesis. *Nat. Commun.* **2020**, *11* (1), 1899.
(17) Creech, M. K.; Wang, J.; Nan, X.; Gibbs, S. L. Superresolution Imaging of Clinical Formalin Fixed Paraffin Embedded Breast Cancer with Single Molecule Localization Microscopy. *Sci. Rep.* **2017**, *7* (1), 40766.
(18) Dempsey, G. T.; Vaughan, J. C.; Chen, K. H.; Bates, M.; Zhuang, X. Evaluation of Fluorophores for Optimal Performance in Localization-Based Super-Resolution Imaging. *Nat. Methods* **2011**, *8* (12), 1027−1036.
(19) Civitci, F.; Shangguan, J.; Zheng, T.; Tao, K.; Rames, M.; Kenison, J.; Zhang, Y.; Wu, L.; Phelps, C.; Esener, S.; Nan, X. Fast and Multiplexed Superresolution Imaging with DNA-PAINT-ERS. *Nat. Commun.* **2020**, *11* (1), 4339.
(20) Koester, A. M.; Szczepaniak, M.; Nan, X. Fast and Multiplexed Super Resolution Imaging of Fixed and Immunostained Cells with DNA-PAINT-ERS. *Curr. Protoc* **2022**, *2* (11), No. e618.
(21) Schueder, F.; Stein, J.; Stehr, F.; Auer, A.; Sperl, B.; Strauss, M. T.; Schwille, P.; Jungmann, R. An Order of Magnitude Faster DNA-PAINT Imaging by Optimized Sequence Design and Buffer Conditions. *Nat. Methods* **2019**, *16* (11), 1101−1104.
(22) Filius, M.; Cui, T. J.; Ananth, A. N.; Docter, M. W.; Hegge, J. W.; van der Oost, J.; Joo, C. High-Speed Super-Resolution Imaging Using Protein-Assisted DNA-PAINT. *Nano Lett.* **2020**, *20* (4), 2264−2270.
(23) Chung, K. K. H.; Zhang, Z.; Kidd, P.; Zhang, Y.; Williams, N. D.; Rollins, B.; Yang, Y.; Lin, C.; Baddeley, D.; Bewersdorf, J. Fluorogenic DNA-PAINT for Faster, Low-Background Super-Resolution Imaging. *Nat. Methods* **2022**, *19*, 554.
(24) Axelrod, D. Cell-Substrate Contacts Illuminated by Total Internal Reflection Fluorescence. *J. Cell Biol.* **1981**, *89* (1), 141−145.
(25) Stout, A. L.; Axelrod, D. Evanescent Field Excitation of Fluorescence by Epi-Illumination Microscopy. *Appl. Opt.* **1989**, *28* (24), 5237−5242.
(26) Silicone Immersion Objectives Boost 3D Live-Cell Imaging. *BioPhotonics*. Olympus: https://www.photonics.com/Articles/Silicone_Immersion_Objectives_Boost_3D_Live-Cell/a62855.
(27) Squires, T. M.; Quake, S. R. Microfluidics: Fluid Physics at the Nanoliter Scale. *Rev. Mod. Phys.* **2005**, *77* (3), 977−1026.
(28) Du, Y.; Wang, C.; Zhang, C.; Guo, L.; Chen, Y.; Yan, M.; Feng, Q.; Shang, M.; Kuang, W.; Wang, Z.; Huang, Z.-L. Computational Framework for Generating Large Panoramic Super-Resolution Images from Localization Microscopy. *Biomed. Opt. Express* **2021**, *12* (8), 4759−4778.
(29) von Diezmann, A.; Lee, M. Y.; Lew, M. D.; Moerner, W. E. Correcting Field-Dependent Aberrations with Nanoscale Accuracy in Three-Dimensional Single-Molecule Localization Microscopy. *Optica* **2015**, *2* (11), 985−993.
(30) Yan, T.; Richardson, C. J.; Zhang, M.; Gahlmann, A. Computational Correction of Spatially Variant Optical Aberrations in 3D Single-Molecule Localization Microscopy. *Opt. Express* **2019**, *27* (9), 12582−12599.
(31) Nan, X.; Tamgüney, T. M.; Collisson, E. A.; Lin, L.-J.; Pitt, C.; Galeas, J.; Lewis, S.; Gray, J. W.; McCormick, F.; Chu, S. Ras-GTP Dimers Activate the Mitogen-Activated Protein Kinase (MAPK) Pathway. *Proc. Natl. Acad. Sci. U. S. A.* **2015**, *112* (26), 7996−8001.
(32) Arganda-Carreras, I.; Kaynig, V.; Rueden, C.; Eliceiri, K. W.; Schindelin, J.; Cardona, A.; Sebastian Seung, H. Trainable Weka Segmentation: A Machine Learning Tool for Microscopy Pixel Classification. *Bioinformatics* **2017**, *33* (15), 2424−2426.
(33) Eliceiri, K. W.; Berthold, M. R.; Goldberg, I. G.; Ibáñez, L.; Manjunath, B. S.; Martone, M. E.; Murphy, R. F.; Peng, H.; Plant, A. L.; Roysam, B.; Stuurman, N.; Swedlow, J. R.; Tomancak, P.; Carpenter, A. E. Biological Imaging Software Tools. *Nat. Methods* **2012**, *9* (7), 697−710.
(34) Anderson, R. G.; Jacobson, K. A Role for Lipid Shells in Targeting Proteins to Caveolae, Rafts, and Other Lipid Domains. *Science* **2002**, *296* (5574), 1821−1825.
(35) Basu Roy, U. K.; Henkhaus, R. S.; Loupakis, F.; Cremolini, C.; Gerner, E. W.; Ignatenko, N. A. Caveolin-1 Is a Novel Regulator of K-RAS-Dependent Migration in Colon Carcinogenesis. *Int. J. Cancer* **2013**, *133* (1), 43−57.
(36) Volonte, D.; Vyas, A. R.; Chen, C.; Dacic, S.; Stabile, L. P.; Kurland, B. F.; Abberbock, S. R.; Burns, T. F.; Herman, J. G.; Di, Y. P.; Galbiati, F. Caveolin-1 Promotes the Tumor Suppressor Properties of Oncogene-Induced Cellular Senescence. *J. Biol. Chem.* **2018**, *293* (5), 1794−1809.
(37) Yang, G.; Sacci, R. L.; Ivanov, I. N.; Ruther, R. E.; Hays, K. A.; Zhang, Y.; Cao, P.-F.; Veith, G. M.; Dudney, N. J.; Saito, T.; Hallinan, D. T.; Nanda, J. Probing Electrolyte Solvents at Solid/Liquid Interface Using Gap-Mode Surface-Enhanced Raman Spectroscopy. *J. Electrochem. Soc.* **2019**, *166* (2), A178−A187.
(38) Fuhrmann, D. C.; Brüne, B. Mitochondrial Composition and Function under the Control of Hypoxia. *Redox Biol.* **2017**, *12*, 208−215.
(39) Yu, M.; Nguyen, N. D.; Huang, Y.; Lin, D.; Fujimoto, T. N.; Molkentine, J. M.; Deorukhkar, A.; Kang, Y.; San Lucas, F. A.; Fernandes, C. J.; Koay, E. J.; Gupta, S.; Ying, H.; Koong, A. C.; Herman, J. M.; Fleming, J. B.; Maitra, A.; Taniguchi, C. M. Mitochondrial Fusion Exploits a Therapeutic Vulnerability of Pancreatic Cancer. *JCI Insight* **2019**, *4*, e126915.
(40) Prieto, J.; León, M.; Ponsoda, X.; Sendra, R.; Bort, R.; Ferrer-Lorente, R.; Raya, A.; López-Garciá, C.; Torres, J. Early ERK1/2 Activation Promotes DRP1-Dependent Mitochondrial Fission Necessary for Cell Reprogramming. *Nat. Commun.* **2016**, *7*, 11124.
(41) Yuen, A.; Díaz, B. The Impact of Hypoxia in Pancreatic Cancer Invasion and Metastasis. *Hypoxia (Auckland, N.Z.)* **2014**, *2*, 91−106.
(42) Stehr, F.; Stein, J.; Schueder, F.; Schwille, P.; Jungmann, R. Flat-Top TIRF Illumination Boosts DNA-PAINT Imaging and Quantification. *Nat. Commun.* **2019**, *10* (1), 1268.

https://doi.org/10.1021/cbmi.3c00060
Chem. Biomed. Imaging 2023, 1, 817−830

(43) Fu, S.; Shi, W.; Luo, T.; He, Y.; Zhou, L.; Yang, J.; Yang, Z.; Liu, J.; Liu, X.; Guo, Z.; Yang, C.; Liu, C.; Huang, Z.-L.; Ries, J.; Zhang, M.; Xi, P.; Jin, D.; Li, Y. Field-Dependent Deep Learning Enables High-Throughput Whole-Cell 3D Super-Resolution Imaging. *Nat. Methods* **2023**, *20* (3), 459−468.
(44) Almada, P.; Pereira, P. M.; Culley, S.; Caillol, G.; Boroni-Rueda, F.; Dix, C. L.; Charras, G.; Baum, B.; Laine, R. F.; Leterrier, C.; Henriques, R. Automating Multimodal Microscopy with NanoJ-Fluidics. *Nat. Commun.* **2019**, *10* (1), 1223.
(45) Klevanski, M.; Herrmannsdoerfer, F.; Sass, S.; Venkataramani, V.; Heilemann, M.; Kuner, T. Automated Highly Multiplexed Super-Resolution Imaging of Protein Nano-Architecture in Cells and Tissues. *Nat. Commun.* **2020**, *11* (1), 1552.
(46) Li, L.; Xin, B.; Kuang, W.; Zhou, Z.; Huang, Z.-L. Divide and Conquer: Real-Time Maximum Likelihood Fitting of Multiple Emitters for Super-Resolution Localization Microscopy. *Opt. Express* **2019**, *27* (15), 21029.
(47) Lin, J.-R.; Fallahi-Sichani, M.; Sorger, P. K. Highly Multiplexed Imaging of Single Cells Using a High-Throughput Cyclic Immunofluorescence Method. *Nat. Commun.* **2015**, *6*, 8390.
(48) Agasti, S. S.; Wang, Y.; Schueder, F.; Sukumar, A.; Jungmann, R.; Yin, P. DNA-Barcoded Labeling Probes for Highly Multiplexed Exchange-PAINT Imaging. *Chem. Sci.* **2017**, *8* (4), 3080−3091.
(49) Oleksiievets, N.; Sargsyan, Y.; Thiele, J. C.; Mougios, N.; Sograte-Idrissi, S.; Nevskyi, O.; Gregor, I.; Opazo, F.; Thoms, S.; Enderlein, J.; Tsukanov, R. Fluorescence Lifetime DNA-PAINT for Multiplexed Super-Resolution Imaging of Cells. *Commun. Biol.* **2022**, *5* (1), 38.
(50) Speiser, A.; Müller, L.-R.; Hoess, P.; Matti, U.; Obara, C. J.; Legant, W. R.; Kreshuk, A.; Macke, J. H.; Ries, J.; Turaga, S. C. Deep Learning Enables Fast and Dense Single-Molecule Localization with High Accuracy. *Nat. Methods* **2021**, *18* (9), 1082−1090.
(51) Szymborska, A.; de Marco, A.; Daigle, N.; Cordes, V. C.; Briggs, J. a. G.; Ellenberg, J. Nuclear Pore Scaffold Structure Analyzed by Super-Resolution Microscopy and Particle Averaging. *Science* **2013**, *341* (6146), 655−658.
(52) Mund, M.; Tschanz, A.; Wu, Y.-L.; Frey, F.; Mehl, J. L.; Kaksonen, M.; Avinoam, O.; Schwarz, U. S.; Ries, J. Clathrin Coats Partially Preassemble and Subsequently Bend during Endocytosis. *J. Cell Biol.* **2023**, *222* (3), e202206038.
(53) Wu, Y.-L.; Hoess, P.; Tschanz, A.; Matti, U.; Mund, M.; Ries, J. Maximum-Likelihood Model Fitting for Quantitative Analysis of SMLM Data. *Nat. Methods* **2023**, *20* (1), 139−148.
(54) Mund, A.; Coscia, F.; Kriston, A.; Hollandi, R.; Kovács, F.; Brunner, A.-D.; Migh, E.; Schweizer, L.; Santos, A.; Bzorek, M.; Naimy, S.; Rahbek-Gjerdrum, L. M.; Dyring-Andersen, B.; Bulkescher, J.; Lukas, C.; Eckert, M. A.; Lengyel, E.; Gnann, C.; Lundberg, E.; Horvath, P.; Mann, M. Deep Visual Proteomics Defines Single-Cell Identity and Heterogeneity. *Nat. Biotechnol.* **2022**, *40*, 1231.
(55) Ouyang, W.; Aristov, A.; Lelek, M.; Hao, X.; Zimmer, C. Deep Learning Massively Accelerates Super-Resolution Localization Microscopy. *Nat. Biotechnol.* **2018**, *36* (5), 460.
(56) Dember, L. M. Amyloidosis-Associated Kidney Disease. *Journal of the American Society of Nephrology* **2006**, *17* (12), 3458.
(57) de Senneville, B. D.; Khoubai, F. Z.; Bevilacqua, M.; Labedade, A.; Flosseau, K.; Chardot, C.; Branchereau, S.; Ripoche, J.; Cairo, S.; Gontier, E.; Grosset, C. F. Deciphering Tumour Tissue Organization by 3D Electron Microscopy and Machine Learning. *Communications Biology* **2021**, *4* (1), 1390.
(58) Riesterer, J. L.; López, C. S.; Stempinski, E. S.; Williams, M.; Loftis, K.; Stoltz, K.; Thibault, G.; Lanicault, C.; Williams, T.; Gray, J. W. A Workflow for Visualizing Human Cancer Biopsies Using Large-Format Electron Microscopy. In *Methods in Cell Biology*; Tran, P., Ed.; Academic Press, 2020; Vol. *158*, pp 163−181.
(59) Edelstein, A. D.; Tsuchida, M. A.; Amodaj, N.; Pinkard, H.; Vale, R. D.; Stuurman, N. Advanced Methods of Microscope Control Using MManager Software. *J. Biol. Methods* **2014**, *1* (2), No. e10.
(60) Nickerson, A.; Huang, T.; Lin, L.-J.; Nan, X. Photoactivated Localization Microscopy with Bimolecular Fluorescence Complementation (BiFC-PALM). *J. Vis. Exp.* **2015**, No. 106, No. e53154.

https://doi.org/10.1021/cbmi.3c00060
Chem. Biomed. Imaging 2023, 1, 817−830